RESEARCH ARTICLE
Editor's Choice
ADVANCED MATERIALS
www.advmat.de

Making Interfacial Solar Evaporation of Seawater Faster than Fresh Water

Huimin Yu, Huanyu Jin, Meijia Qiu, Yunzheng Liang, Peng Sun, Chuanqi Cheng, Pan Wu, Yida Wang, Xuan Wu, Dewei Chu, Min Zheng, Tong Qiu, Yi Lu, Bin Zhang, Wenjie Mai, Xiaofei Yang,* Gary Owens, and Haolan Xu**

Interfacial solar evaporation-based seawater desalination is regarded as one of the most promising strategies to alleviate freshwater scarcity. However, the solar evaporation rate of real seawater is significantly constricted by the ubiquitous salts present in seawater. In addition to the common issue of salt accumulation on the evaporation surface during solar evaporation, strong hydration between salt ions and water molecules leads to a lower evaporation rate for real seawater compared to pure water. Here a facile and general strategy is developed to reverse this occurrence, that is, making real seawater evaporation faster than pure water. By simply introducing specific mineral materials into the floating photothermal evaporator, ion exchange at air–water interfaces directly results in a decrease in seawater evaporation enthalpy, and consequently achieves much higher seawater evaporation rates compared to pure water. This process is spontaneously realized during seawater solar evaporation. Considering the current enormous clean water production from evaporation-based desalination plants, such an evaporation performance improvement can remarkably increase annual clean water production, benefiting millions of people worldwide.

1. Introduction

Freshwater is a strategically important resource. However, freshwater scarcity currently threatens the survival and development of humankind. Today, 1.8–2.9 billion people are suffering from severe freshwater shortages for at least 4 months of the year,[1,2] and the situation is likely to get worse in the future. It is predicted that by 2050 global freshwater demand will further increase by 19%, and consequently 75% of the global population will face clean water shortages.[3] Seawater desalination is the most effective strategy to alleviate the impending freshwater scarcity owing to Earth's abundant seawater reserves. Some technologies have been successfully applied to desalinate seawater, including membrane filtration, thermal distillation, and reverse osmosis, but all require massive energy consumption on a large scale

H. Yu, Y. Liang, P. Wu, Y. Wang, X. Wu, G. Owens, H. Xu
Future Industries Institute
UniSA STEM
University of South Australia
Mawson Lakes Campus
Adelaide, SA 5095, Australia
E-mail: haolan.xu@unisa.edu.au
H. Jin
Institute of Technology for Carbon Neutrality
Shenzhen Institute of Advanced Technology
Chinese Academy of Sciences
Shenzhen, Guangdong 518055, China
M. Qiu, P. Sun, W. Mai
Siyuan Laboratory
Guangzhou Key Laboratory of Vacuum Coating Technologies and New Energy Materials
Guangdong Provincial Engineering Technology Research Center of Vacuum Coating Technologies and New Energy Materials
Department of Physics
Jinan University
Guangzhou 510632, China
E-mail: wenjiemai@E-mail.jnu.edu.cn
The ORCID identification number(s) for the author(s) of this article can be found under https://doi.org/10.1002/adma.202414045

DOI: 10.1002/adma.202414045

C. Cheng, B. Zhang
Department of Chemistry
School of Science
Tianjin University
Tianjin 300072, China
D. Chu
School of Materials Science and Engineering
University of New South Wales
Sydney NSW 2052, Australia
M. Zheng
School of Chemical Engineering and Advanced Materials
University of Adelaide
Adelaide, SA 5005, Australia
T. Qiu
Materials Industrialization Engineering Research Center
School of Materials Science and Engineering
Shanghai Jiao Tong University
Shanghai 200240, China
Y. Lu, X. Yang
Jiangsu Co-Innovation Center of Efficient Processing and Utilization of Forest Resources
International Innovation Center for Forest Chemicals and Materials
College of Science
Nanjing Forestry University
Nanjing 210037, China
E-mail: xiaofei.yang@njfu.edu.cn

and hence have large carbon footprints.[4–6] In comparison, solar-powered evaporation, especially the recently developed interfacial solar evaporation, has shown great potential as a promising alternative desalination technology due to the considerable merits of using a sustainable solar energy source, green evaporation processes, and excellent water evaporation performance.[7–11]

Improving the evaporation rate is one of the most important elements for pushing forward the practical applications of interfacial solar evaporation for seawater desalination. So far, energy efficiencies of interfacial solar evaporation and evaporation rates have been significantly improved by a range of strategies of preparing high-performance photothermal materials, rationally designing evaporators, lowering evaporation enthalpy, and optimizing thermal energy management during interfacial solar evaporation.[12–33] For practical solar evaporation of real seawater, salt content in natural seawater brings practical issues such as salt fouling on evaporation surfaces, which blocks light absorption and water transportation, thus degrading evaporation performance. To address this critical issue, several effective problem-solving solutions have been developed and testified. For example, creating sufficient ion transport channels to boost ion diffusion capacity to alleviate the salt precipitation.[27,34–41] Alternatively, salt-resistant properties can be achieved by incorporating a Janus hydrophilic–hydrophobic structure to segregate water transportation and evaporation regions.[42–49] Selective regional salt crystallization and self-rotating evaporators have also been designed to achieve long-term stable seawater evaporation.[50–54]

However, while salt scaling can be solved by these methods, the salt ions in seawater have another negative effect on the solar evaporation rate. The intrinsic strong hydration between salt ions and water molecules leads to an increase in evaporation enthalpy and hinders the escape of water molecules from the seawater surface to the air, resulting in lower evaporation rates compared to that of pure water evaporation.[55–57] This phenomenon is generally well-known and has been commonly reported. Typically, the evaporation rate of seawater/saline water is ~8.0% lower than that of pure water, as observed in most of the previously reported interfacial solar evaporation and thermal distillation processes (Table S1, Supporting Information). Taking pure water evaporation as a benchmark, if one can make initially slower seawater evaporation become faster than pure water evaporation, it will substantially increase both absolute seawater evaporation rate and clean water yield. Realizing this advance would represent a major step forward solving freshwater scarcity. Considering the huge annual desalination market and clean water production from evaporation-based desalination plants (≈6.7 billion m^3 per year),[58] even small declines in desalination performance could potentially result in the loss of tens of millions of tons of clean water. Therefore, it is significantly meaningful to develop a strategy to improve the evaporation rate of seawater to reach or exceed the evaporation rates of pure water. This will directly result in additional access to massive amounts of clean water for millions of people worldwide.

Recently, Lei et al.[24] and Zou et al.[59] reported faster evaporation of NaCl brine than pure water by regulating polymeric network–water interactions and Hofmeister effect, respectively. Different from NaCl solution, real seawater has a more complex ionic environment. We found that not all the major cations in seawater (i.e., Na^+, K^+, Mg^{2+}, Ca^{2+}) give rise to lowered evaporation rates of seawater. The dark evaporation tests of the single salt solutions at the same concentrations in natural seawater (0.529 M NaCl, 0.027 M KCl, 0.021 M $CaCl_2$, and 0.064 M $MgCl_2$) revealed that compared to the pure water evaporation, while Na^+ significantly decreased the evaporation rate, Mg^{2+} and Ca^{2+} remarkably increased the evaporation rate (Figure S1, Supporting Information). Since the concentration of Na^+ in seawater is much higher than that of Mg^{2+} and Ca^{2+}, the dominant negative effect of Na^+ makes seawater evaporation slower than pure water. However, during interfacial solar evaporation, if a floating evaporator can selectively enrich Mg^{2+} and Ca^{2+} in seawater to the evaporation surfaces, it is possible to significantly improve the seawater evaporation rate even over pure water evaporation rate. Based on this consideration, here we developed a simple and cost-effective method to reverse the deficit in the evaporation rate of seawater, that is, realizing faster interfacial solar evaporation of real seawater compared to pure water. This was achieved by simply introducing mineral materials, such as halloysite nanotubes (HNTs), bentonite (BN), zeolite (ZL), and montmorillonite (MN) into the photothermal hydrogel evaporator composed of carbon nanotubes (CNTs, as the light absorber) and sodium alginate (SA, as the structural framework). During interfacial solar evaporation, the mineral component in the floating evaporator could enrich Mg^{2+} and Ca^{2+} by ion exchange with the ubiquitous cations of Mg^{2+} and Ca^{2+} in seawater,[60] which surprisingly decreased the evaporation enthalpy of seawater, thus boosting seawater evaporation (**Figure 1a**). Consequently, this work realized much higher evaporation rates for seawater than that of pure water. More importantly, this process occurs spontaneously during solar evaporation of seawater without any special treatment, making this strategy extremely convenient and cost-effective for practical applications.

2. Results and Discussion

2.1. Selective Ion Exchange between the HNT and Mg^{2+}, Ca^{2+} in Seawater

Taking the HNT as an example, it has a layered structure composed of different compositions at observe (—Al—OH) and reserve (—O—Si—O) surfaces rolled into a nanotube morphology (Figure S2, Supporting Information), where the Al^{3+} cation can be exchanged with a number of different cations.[60] The ion exchange between the Al^{3+} in HNT and main cations (i.e., Na^+, K^+, Ca^{2+}, and Mg^{2+}) in seawater was investigated first. Ion exchange typically occurs between ions with similar charge numbers and ionic radii.[60,61] The charge numbers of Mg^{2+} and Ca^{2+} are closer to Al^{3+} compared to K^+ and Na^+ in seawater. In addition, the radii of Mg^{2+}, Ca^{2+}, K^+, and Na^+ are 109, 148, 162, and 123 pm, respectively, where the radius of Mg^{2+} is the closest to Al^{3+} (98 pm). Therefore, the ion exchange is likely to occur predominantly between Mg^{2+} and Al^{3+}. The ab initio molecular dynamics (AIMD) simulations were conducted to elucidate the ion exchange process. The evolution of the distances between the selected oxygen in HNT and Mg^{2+}, Al^{3+} was monitored over simulation time (Figure 1b). When Mg^{2+} in seawater approached

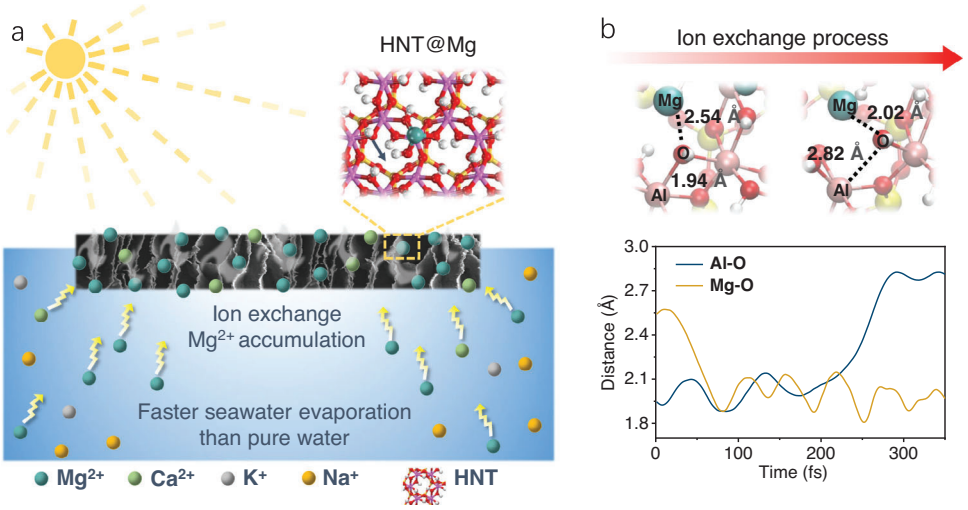

Figure 1. a) Schematic illustration of enrichment of Mg^{2+} on evaporation surfaces by spontaneous ion exchange between Al^{3+} in HNT and Mg^{2+} in seawater for faster seawater evaporation than pure water. b) The snapshots of different structures before (left) and after (right) the Al^{3+}–Mg^{2+} ion exchange process (O, H, Al, Si, Mg in red, white, pink, yellow, and cyan, respectively). Evolution of Al—O and Mg—O bond distance of one selected ion exchange site as a function of time.

the HNT surface, the Mg—O distance kept decreasing until the Mg—O bond formed and stabilized into an oscillating state. Conversely, the Al—O distance began to increase after 200 fs, reaching over 2.8 Å after 350 fs, confirming the break of Al—O bonds and the ion exchange between Mg^{2+} and Al^{3+}. Similar trends were observed in Ca—O and Al—O distance plots but at a slower pace, suggesting a weaker ion exchangeability between Ca^{2+} and Al^{3+} (Figure S3, Supporting Information). The ion exchange between Na^{+} and Al^{3+} was also investigated (Figure S4, Supporting Information). No Na—O bond was formed while the Al—O bond exhibited stable fluctuations without a bond break, indicating that Na^{+} did not exchange with Al^{3+} in HNTs. The calculated adsorption energy between the cations in seawater and HNTs followed the order of $Mg^{2+} < Ca^{2+} < Na^{+} < K^{+}$ (**Figure** 2a,b), indicating that Mg^{2+} has the most significant adsorption ability on the surface of HNT, which is favorable for subsequent ion-exchange steps. Moreover, assuming Mg^{2+}, Ca^{2+}, Na^{+}, and K^{+} all successfully exchanged with Al^{3+} in HNT structure, the dissociation energy of the formed metal–oxygen bond followed the order of $Mg^{2+} > Ca^{2+} > Na^{+} > K^{+}$ (Figure 2c), confirmed that the stability of Mg^{2+}-HNT after ion exchange was the highest. Inductively coupled plasma optical emission spectroscopy (ICP-OES) analysis confirmed selective ion exchange between the HNTs (i.e., Al^{3+}) and Mg^{2+}, Ca^{2+} in seawater (Figure 2d). After rinsing in seawater, the Al^{3+} content in HNTs decreased, while the Ca^{2+} and Mg^{2+} contents both significantly increased. Specifically, the increase in Mg^{2+} content was the greatest, aligning with the simulation results. Therefore, the HNTs exhibited a strong capability to exchange Al^{3+} with Mg^{2+} to accumulate Mg^{2+} on the surfaces, despite the initial concentration of Mg^{2+} in seawater is not the highest. Since Mg^{2+} can improve water evaporation rate (Figure S1, Supporting Information), if the HNTs are loaded in a photothermal evaporator floating on seawater surfaces, the enriched Mg^{2+} on evaporation surfaces should be able to boost the seawater evaporation rate.

2.2. Characterizations and Solar Evaporation Performances of HNT-Photothermal Hydrogels

The HNT-photothermal hydrogel was synthesized by gelation of a well-dispersed mixture of HNTs, CNTs, and SA, followed by freezing drying, and crosslinking, to explore the effect of ion exchange for solar evaporation performance. The obtained photothermal hydrogel showed low density with vertically aligned layered structures (Figure 2e), providing channels for water transportation, vapor escape, and salt diffusion during solar evaporation. The HNTs were randomly distributed on the hydrogel walls (Figure S5, Supporting Information). X-ray photoelectron spectroscopy (XPS), Fourier transform infrared (FTIR) spectra, and X-ray diffraction (XRD) analysis confirmed the integration of HNT, CNT, and SA into the hydrogel (Figure S6, Supporting Information). The obtained HNT-photothermal hydrogel showed good mechanical strength for interfacial solar evaporation (Figure S7, Supporting Information). The CNT renders the hydrogel excellent photothermal property. The surface temperature reached 65.9 °C under 1.0 sun irradiation in air (Figure S8, Supporting Information). The light absorption efficiency of the hydrogel can be up to ≈97% in a wet state (Figure S9, Supporting Information).[62] The obtained photothermal hydrogel showed excellent hydrophilicity and water transportation, providing a continuous water supply for solar evaporation (Note S1, Figures S10,S11, Supporting Information).

The solar evaporation performance of the HNT-photothermal hydrogel was evaluated under one sun illumination (Figure 2f). The solar evaporation rate for pure water using the HNT-photothermal hydrogel was 1.76 kg m^{-2} h^{-1} (Figure 2g). Accepted practice suggests that the evaporation rate for a salt solution should be less. However, the HNT-photothermal hydrogel delivered a higher evaporation rate of 2.09 kg m^{-2} h^{-1} for real seawater with a lower surface temperature (Figures S12,S13, Supporting Information), which is 18.9% higher than that of pure

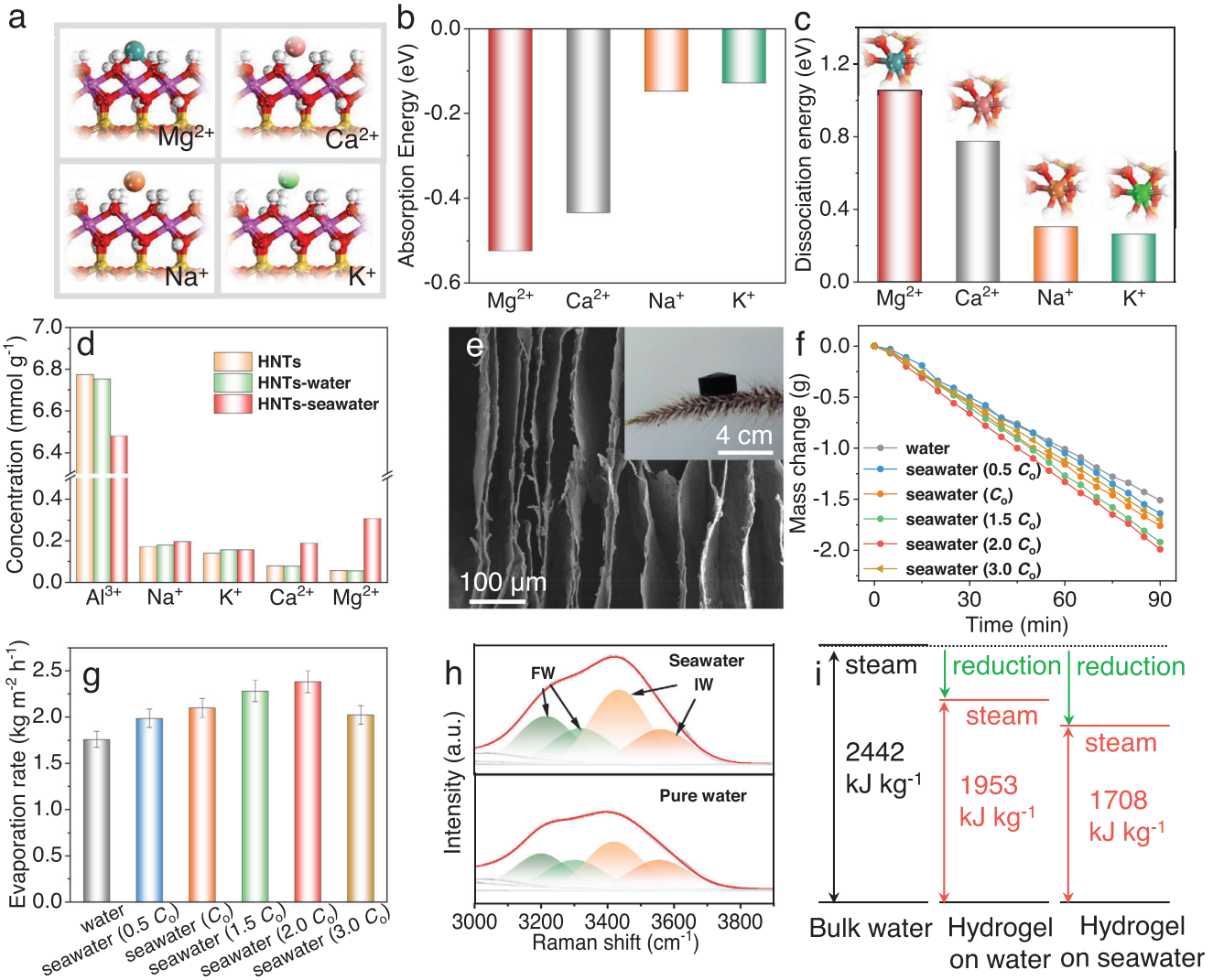

Figure 2. Evaporation performance of the HNT-photothermal hydrogel. a) Structure models of HNT-cation interactions (O, H, Al, Si, Mg, Ca, Na, K in red, white, purple, yellow, cyan, pink, orange, and green, respectively). b) The corresponding DFT calculated absorption energy between Mg^{2+}, Ca^{2+}, Na^{+} and K^{+} and HNT. c) The DFT calculated four metal–oxygen bond dissociation energy for HNT with one Al substituted by another ion including Mg^{2+}, Ca^{2+}, Na^{+}, or K^{+}. d) Ion concentrations of the original, water-treated, and seawater-treated HNTs. e) SEM image, inset: photograph of the hydrogel. f) Mass loss of water and different concentrated seawater during interfacial solar evaporation under one sun. g) Evaporation rate of water and different concentrated seawater under one sun. h) Raman spectrum showing the fitting peaks of IW and FW in the HNT-photothermal hydrogel with seawater and pure water, respectively. i) Schematic illustration of reduction in evaporation enthalpy of the HNT-photothermal hydrogel in pure water and seawater.

water. The improved seawater evaporation could be attributed to the enrichment of Mg^{2+} on evaporation surfaces by the selective ion exchange processes during seawater evaporation. We monitored the time-dependent concentrations of Mg^{2+} in the HNT-photothermal hydrogel throughout the interfacial solar evaporation processes (Figure S14, Supporting Information), which revealed that Mg^{2+} started to enrich in the hydrogel during the initial 30 mins, after which it reached saturation state. This result suggested that the ion exchange between Al^{3+} in HNT and Mg^{2+} in seawater was completed within the first 30 mins of the seawater evaporation process. More surprisingly, the evaporation rate of seawater actually increased when the seawater was concentrated (Figure 2g). For instance, when the initial seawater (C_0) was concentrated to 1.5 and 2 C_0, the solar evaporation rate increased from 2.09 to 2.28 and 2.38 kg m^{-2} h^{-1} respectively, much higher than that of pure water (1.76 kg m^{-2} h^{-1}). The evaporation rate slightly decreased to 2.02 kg m^{-2} h^{-1} when the seawater was further concentrated to 3 C_0, which was still higher than that of pure water. The change in the evaporation rates of different concentrated seawater is due to the different concentrations of Mg^{2+} (positive to seawater evaporation rate) and Na^{+}, K^{+} (negative to seawater evaporation rate) on evaporation surfaces. The concentration of Mg^{2+} on evaporation surfaces is determined by the ion exchange between the Al^{3+} in HNT and Mg^{2+} seawater, while the concentration of Na^{+} and K^{+} directly increases with the increase in seawater concentration. Limited by the ion exchange capacity, when the seawater concentration increased, the increase in Mg^{2+} concentration was

smaller compared to that of Na^+ and K^+ (Figure S15, Supporting Information). Therefore, the positive effect of Mg^{2+} can't offset the negative effect of Na^+, K^+ in 3 C_0 seawater, leading to a slower evaporation rate of 3 C_0 seawater than 2 C_0 seawater. The HNT-photothermal hydrogel was tested before and after immersion in seawater for one month. The evaporation performance remained unchanged, which confirmed the excellent stability of the hydrogel after ion exchange (Figure S16, Supporting Information). During long-term evaporation tests (90 h across 15 days), the HNT-photothermal hydrogel demonstrated good stability in terms of evaporation performance and structure (Figures S17,S18, Supporting Information). Even after immersing the HNT-photothermal hydrogel in seawater for 4 months, no structural damage or deformation was observed (Figure S19, Supporting Information). Outdoor tests were carried out to assess the water evaporation and collection performance under natural sunlight. A home-made device was designed and fabricated to accommodate six HNT-photothermal hydrogel evaporators (Figure S20a–c, Supporting Information). Weather conditions during the outdoor evaporation tests were recorded (Figure S20d, Supporting Information). Over 8 h of outdoor solar evaporation, 51.45 g of clean water was collected, corresponding to a water collection rate of 12.16 kg m^{-2}. The concentrations of Na^+, K^+, Ca^{2+}, and Mg^{2+} in the collected condensed water were much lower than the guideline salinity levels for drinkable desalination water (Figure S21, Supporting Information).[63]

2.3. Mechanism of the Faster Evaporation in Seawater than Pure Water

To exclude the possible effect of the SA hydrogel on accelerating seawater evaporation, HNTs and CNTs were directly deposited on a piece of filtration paper to produce an HNT-CNT film without SA hydrogel. The solar evaporation rate for seawater over this HNT-CNT film was still higher than that of pure water (Figure S22, Supporting Information), confirming that the higher seawater evaporation rate did not originate from the SA hydrogel. For comparison, a photothermal hydrogel with only CNTs and SA (denoted as N-hydrogel) was also prepared (Note S2, Figure S23, Supporting Information). As was observed with many previous studies, without the presence of the HNTs, the N-hydrogel had a 9.8% lower solar evaporation rate (1.47 kg m^{-2} h^{-1}) for seawater compared to the pure water (1.63 kg m^{-2} h^{-1}), which indicated that it was the enriched Mg^{2+}, Ca^{2+} after the ion exchange between HNTs and Mg^{2+}, Ca^{2+} in seawater making the solar evaporation of seawater faster than that of pure water. To further verify this hypothesis, artificial seawater without Mg^{2+} was prepared and tested. The evaporation rate for this artificial seawater remarkably decreased to levels similar to that of pure water (Figure S24, Supporting Information). If both Mg^{2+} and Ca^{2+} were removed from the artificial seawater, the evaporation rate was further reduced and became much lower than that of pure water. These results confirmed that the enrichment of Mg^{2+} and Ca^{2+} via ion exchange between HNTs and seawater led to faster seawater evaporation than pure water. Moreover, HNT-photothermal hydrogels with different HNT contents were prepared to demonstrate the positive effect of the HNTs on seawater evaporation. The seawater evaporation rate increased from 2.09 to 2.78 kg m^{-2} h^{-1} with an increase in HNT content from 500 to 1000 mg (Figure S25, Supporting Information). To further demonstrate the effect of enriched Mg^{2+} after ion exchange on evaporation rate, we directly immersed the pristine HNT-photothermal hydrogel in a 0.064 M $MgCl_2$ solution for 24 h to artificially introduce Mg^{2+} into the hydrogel. Following this treatment, the hydrogel was retested with pure water, resulting in an increased evaporation rate from 1.76 to 2.02 kg m^{-2} h^{-1} (Figure S26, Supporting Information).

Raman analysis was conducted to identify any changes in the water state of the pure water and seawater in the HNT-photothermal hydrogel. The water constrained within the HNT-photothermal hydrogel network can be classified into three types according to the different hydrogen bonds (HB): bound water (BW); intermediate water (IW); and free water (FW).[20] Commonly, BW is strongly bound to surfaces/ions (such as water molecules in the first solvation shell) and is less prone to evaporate, while FW (water molecules beyond the second solvation shell) is less affected by ions and behaves more like bulk water. IW characterized by weak interactions with surfaces/ions and less HB with other water molecules (probably located in the second solvation shell) mainly contributes to the observed difference in water evaporation rates. Raman spectrum of the seawater within the HNT-photothermal hydrogel revealed peaks of FW at 3212, 3316 cm^{-1} and IW at 3434, 3558 cm^{-1} in the region of O—H stretching (Figure 2h). The ratio of IW to FW was 1.295, which was much higher than that of pure water (1.055) in the HNT-photothermal hydrogel network (Figure 2h). Since IW involves only weak hydration, higher IW content contributes to a lower evaporation enthalpy, leading to a higher evaporation rate.[20] The equivalent water evaporation enthalpies for free pure water, and pure water, seawater constrained in the HNT-photothermal hydrogel were measured using dark evaporation experiments (Note S3, Figure S27, Supporting Information), which were 2442, 1953, and 1708 kJ kg^{-1}, respectively (Figure 2i). The evaporation enthalpy of seawater in the HNT-photothermal hydrogel was much lower than that of the pure water in the same hydrogel. Based on the measured evaporation enthalpy, energy efficiencies of the HNT-photothermal hydrogel for seawater and pure water evaporation were calculated (Note S4, Supporting Information). Differential scanning calorimetry (DSC) analysis also confirmed a lower evaporation enthalpy for seawater compared to pure water in the HNT-photothermal hydrogel (Note S5, Figure S28, Supporting Information). The dark evaporation experiments also confirmed the decrease in seawater evaporation enthalpy with the increase in HNT content (Figure S29, Supporting Information), where more Mg^{2+} were enriched at the air–water interfaces.

To reveal the underlying mechanism of the influence of cations in seawater on water evaporation, molecule dynamics (MD) simulations were carried out to investigate the ion-specific effect on the distributed situation of water molecules and their intrinsic interactions. Four model solutions consisting of Na^+, K^+, Ca^{2+}, or Mg^{2+} were built for the simulations (**Figure 3a**). Radical distribution functions (RDF) analysis was conducted to elucidate the local structure of water molecules in these simulated solutions. As depicted in Figure 3b, the RDF of Mg^{2+} exhibited a much stronger and well-defined peak at 2.06 Å associated with the first solvation shell compared to all other cations. The variation in solvation of different cations further impacted the water–water

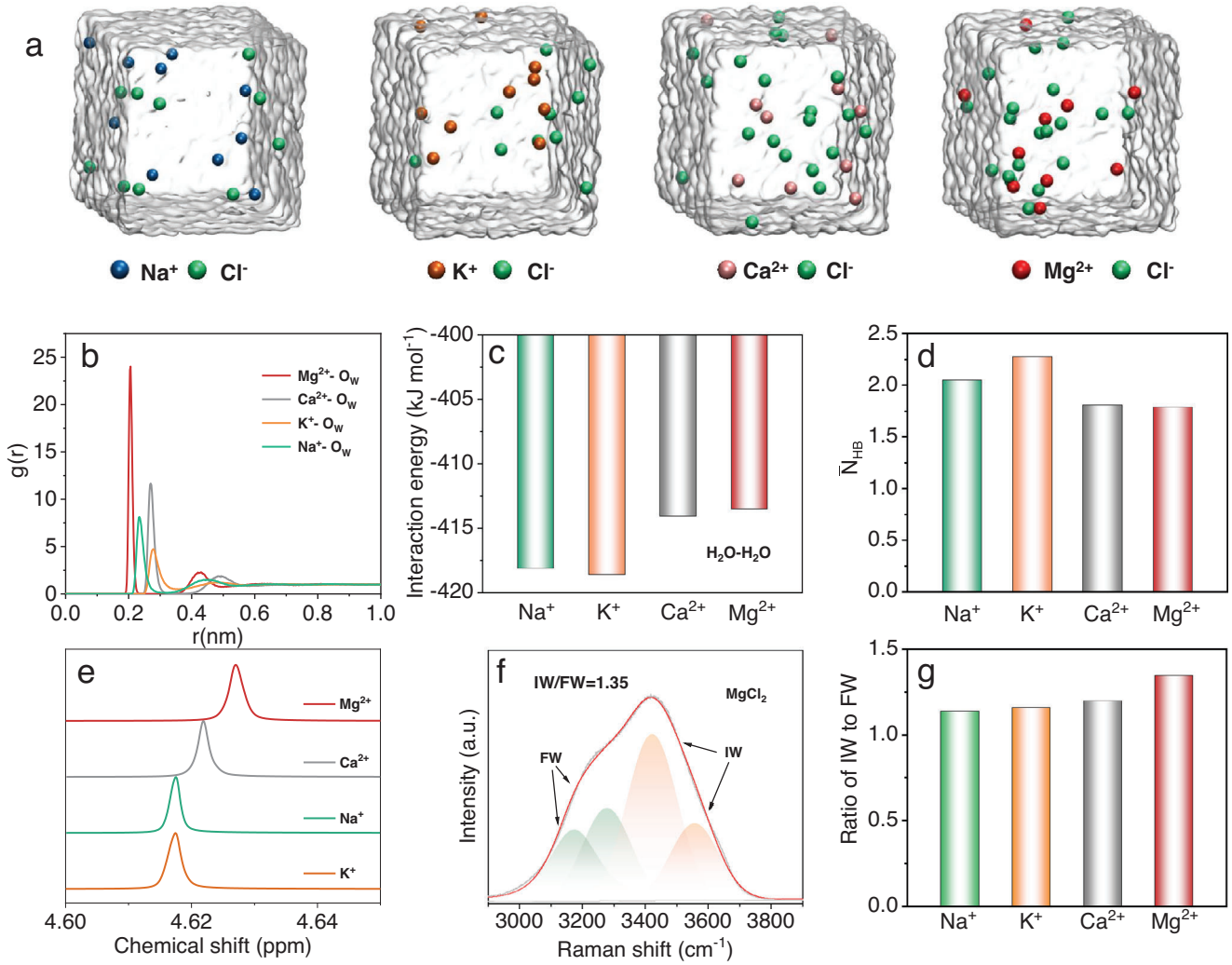

Figure 3. Mechanism of the faster evaporation of seawater than pure water. a) Four different model salt solutions for MD simulations. b) The RDF between different cations and O atoms of water. c) The interaction energy between all water molecules in different solutions. d) Average HB number of water molecules in the first and second solvation shells of Na^+, K^+, Ca^{2+}, Mg^{2+}. e) ^1H NMR spectra of the four solutions. f) Raman spectrum showing the fitting peaks of IW and FW of the $MgCl_2$ solution. g) Ratios of IW to FW of the four salt solutions.

interactions (Figure 3c). The pronounced solvation effect of Mg^{2+} led to a substantial weakening of the interactions between water molecules compared to other cations (Figure 3c), illustrating that Mg^{2+} had the greatest ability to disrupt the pristine water structures. In good agreement with the above results, the average HB number ($\bar{N}_{HB}$) of the water molecules in the first and second solvation shells followed the order of $K^+ > Na^+ > Ca^{2+} > Mg^{2+}$ (Figure 3d). This explained the better evaporation behavior of water with Mg^{2+} than that with Na^+, and K^+ because water molecules with weaker intermolecular interactions and fewer HB numbers are more conducive to reducing the evaporation enthalpy.

Nuclear magnetic resonance (NMR) was also employed to investigate changes in HB amongst water molecules (Figure 3e). Notably, the ^1H peak of water molecules in different solutions was shifted to a lower field position following the order of $K^+ < Na^+ < Ca^{2+} < Mg^{2+}$. This suggested that Mg^{2+} induced the most pronounced disruption to the original HB network of FW, consistent with the MD simulation results. Low-field NMR (LF-NMR) spectra were further measured to investigate the relaxation dynamics and distribution status of water in different salt solutions (Figure S30, Supporting Information). The Mg^{2+} solution showed the lowest FW content and the highest IW content. In addition, Raman spectra also confirmed that the $MgCl_2$ solution exhibited the highest ratio of IW/FW (Figure 3f,g; Figure S31, Supporting Information), which agreed well with the NMR results. Collectively, these results confirmed that Mg^{2+} is more effective than K^+, Na^+, and Ca^{2+} in disturbing HB of water to lower the evaporation enthalpy.

MD simulations were further conducted to mimic the solar evaporation behavior of pure water and seawater in the presence of HNT-photothermal hydrogel (Note S6, Figures S32,S33, Supporting Information). The snapshots showed different evaporation behaviors of water and seawater on the surfaces of the original HNT and ion-exchanged HNT (**Figure 4**; Figures S34,S35, Supporting Information). A total of 378 water molecules were

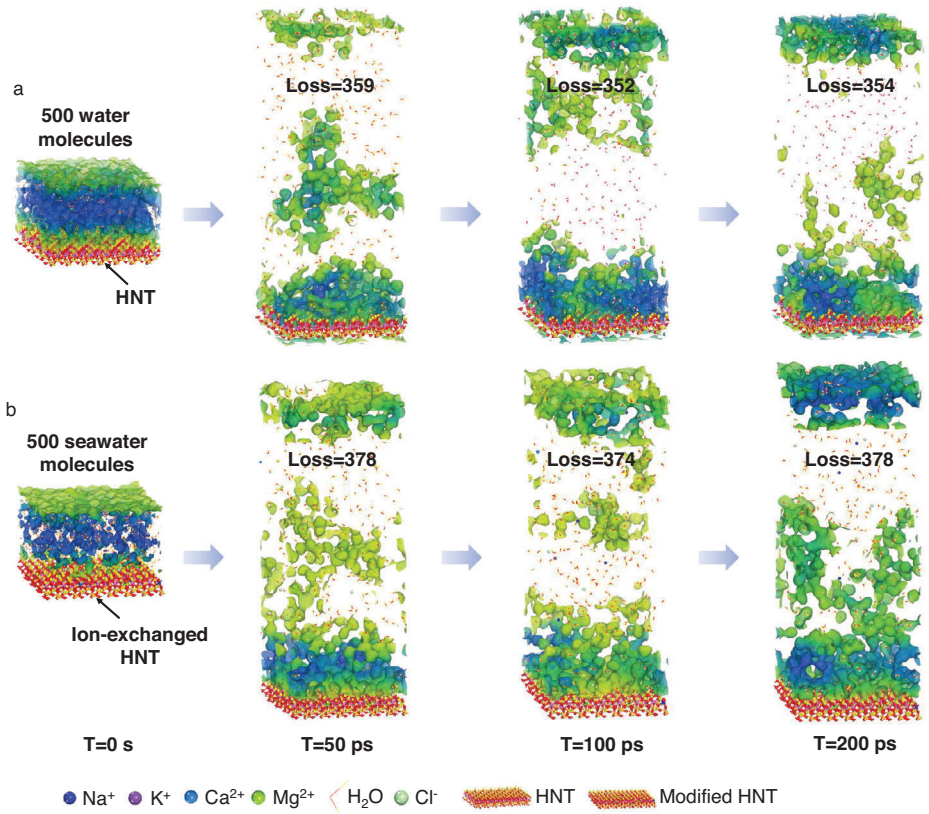

Figure 4. a) Snapshots of water loss on the original HNT surface and b) seawater loss on ion-modified HNT surface at 0, 50, 100, and 200 ps, respectively.

lost from seawater on the surface of the ion-exchanged HNT at 200 ps, while only 354 water molecules were lost from pure water on the surface of the original HNT. These results confirmed the improved evaporation performance of seawater over HNT after ion exchange, which agreed well with the experimental results (Figure 3c). In addition, simulation results also confirmed that the seawater evaporation over the ion-exchanged HNT was also faster than that over the original HNT (353 water loss, Figures S36,S37, Supporting Information), further confirming that the Mg^{2+}, Ca^{2+} enrichment after ion exchange is the main reasons making the seawater evaporation faster than pure water evaporation.

2.4. Universality of the Strategy for Faster Evaporation of Seawater than Pure Water

To investigate the universality of the mechanism for enhancing the evaporation rate of seawater relative to pure water, three other minerals (BN, ZL, and MN) with ion exchange capability were also investigated. The phase structures of these minerals were investigated by XRD (Figure S38, Supporting Information). Using the same synthetic method for HNT-photothermal hydrogel fabrication, BN, ZL, and MN-photothermal hydrogels were prepared for evaporation tests. **Figure** 5a–c confirmed the formation of similar vertically aligned channels for these hydrogels. After immersing in seawater, the Mg^{2+} enrichment was observed in all the BN, ZL, and MN-photothermal hydrogels (Figure 5d–f). As expected, these three hydrogels also showed higher evaporation rates for seawater relative to pure water (Figure 5g–i; Figure S39, Supporting Information). From these results, we can conclude that by this simple, spontaneous, and general strategy, Mg^{2+} ions in seawater can be enriched on the photothermal evaporation surfaces (i.e., air–water interfaces), which significantly improves the evaporation rate of real seawater, making it even faster than pure water evaporation. This strategy is also applicable to other photothermal materials and evaporators. For example, by simply adding HNTs into rGO-SA and CNT-PVA photothermal hydrogels (Notes S7,S8, Supporting Information), the obtained HNT-rGO-SA and HNT-CNT-PVA hydrogels all showed faster seawater evaporation than pure water evaporation (Figures S40,S41, Supporting Information). In addition to the above 2D evaporators, we also fabricated different 3D evaporators by coating HNTs, CNTs, and SA on 3D sponge surfaces (Note S9, Supporting Information) and wrapping HNTs and CNTs-coated bamboo paper on a cotton cylinder (Note S10, Supporting Information). The obtained HNT-sponge 3D evaporator showed a seawater evaporation rate of 4.63 kg m^{-2} h^{-1}, which was higher than that of pure water (4.00 kg m^{-2} h^{-1}, Figure S42, Supporting Information). Similarly, the HNT-cotton 3D evaporator also delivered a higher evaporation rate for seawater (4.91 kg m^{-2} h^{-1}) relative to pure water (4.15 kg m^{-2} h^{-1}, Figure S43, Supporting Information), confirming the generality of this strategy. Large-sized photothermal materials can also be fabricated by a modified spray coating method to target large-scale applications (Figure S44, Note S11, Supporting Information).

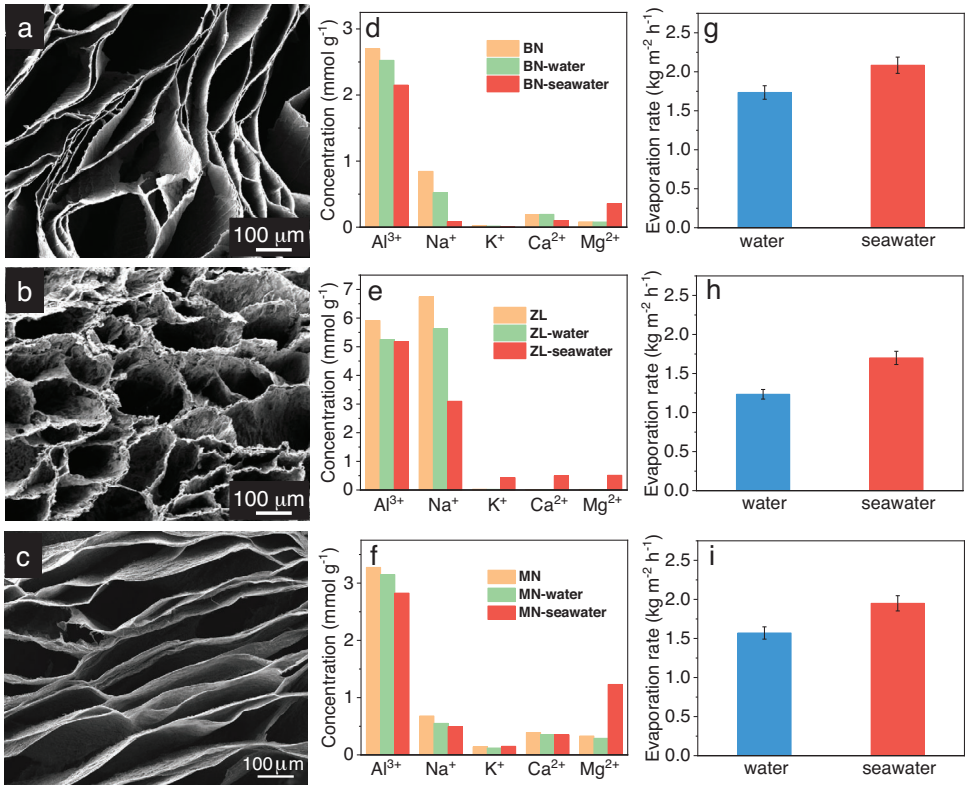

Figure 5. The universality of the strategy for faster evaporation of seawater than pure water. Cross-section SEM images of a) BN, b) ZL, and c) MN-photothermal aerogels. Ion concentrations of original, water-treated, and seawater-treated d) BN, e) ZL, and f) MN. Evaporation rates of water and seawater of g) BN, h) ZL, and i) MN-photothermal hydrogels.

In addition to interfacial solar evaporation, we also tested the thermal distillation behavior of the HNT-photothermal hydrogels in pure water and seawater at 50, 60, and 70 °C, respectively (Note S12, Figure S45, Supporting Information). The evaporation rates of the HNT-hydrogel in pure water were 1.12, 1.60, and 2.32 kg m^{-2} h^{-1} at 50, 60, and 70 °C, respectively. In comparison, the evaporation rates of the hydrogel in seawater increased to 1.29, 1.80, and 2.48 kg m^{-2} h^{-1} at 50, 60, and 70 °C, respectively, which were higher than that of pure water at the same temperatures. This result indicated that this strategy could also be generally extended to thermal distillation-based seawater desalination. Considering the huge capacity of the current evaporation-based seawater desalination, it is thus expected that this technology could remarkably increase clean water production annually.

3. Conclusion

A new facial and effective strategy was developed to make seawater evaporation faster than pure water evaporation by the simple addition of inexpensive and ubiquitous clay minerals to the photothermal hydrogel. Enhanced evaporation of seawater occurred because Mg^{2+} and Ca^{2+} ions in seawater can be accumulated at the photothermal interfaces by spontaneous ion exchange, which directly disturbed the HB of water molecules, leading to a reduction in the evaporation enthalpy and consequentially much faster seawater evaporation compared to pure water. Furthermore, this mechanism for seawater evaporation enhancement seems generally applicable to a range of minerals (e.g., HNT, BN, ZL, and MN) that share similar ion adsorption and exchange capabilities. In addition, this strategy has been verified in various material systems and evaporators. In this work, without the addition of ion exchange clay to the photothermal hydrogel, the seawater evaporation was 9.8% slower than that of pure water evaporation. However, with the addition of HNTs (i.e., HNT-photothermal hydrogel), seawater evaporation became 18.8% faster than pure water evaporation. This simple amendment to photothermal hydrogel fabrication by adding the required low-cost Mg^{2+} absorbing minerals (Note S13, Table S2, Supporting Information) has the potential to significantly improve practical clean water production from existing evaporation-based seawater desalination technologies, benefiting millions of people worldwide currently suffering from water insecurity.

4. Experimental Section

Materials and Chemicals: Halloysite nanotubes (HNTs), bentonite (BN), zeolite (ZL), sodium alginate (SA), and sodium dodecylbenzenesulfonate (SDBS) were purchased from Sigma-Aldrich. $AlCl_3$ was purchased from Chem-Supply. Carbon nanotubes (CNTs) were purchased from Blue Nano, China. Unless otherwise indicated, Milli-Q water with a resistance >18.2 MΩ cm^{-1} was used for all experiments.

Preparation of HNT-CNT-SA Dispersion: Initially, a 25 mg mL^{-1} SA solution was prepared by heating and magnetic stirring a mixture of SA powders (2.5 g) and water (100 mL) at 80 °C for 2 h. Then, 20 mg CNTs and

20 mg SDBS were dispersed in 8 mL water with ultrasonication for 30 min. HNTs (500 mg) were added into the CNT dispersion and ultrasonicated for another 10 min. Finally, the SA dispersion (2 mL) was added into the above prepared CNT–HNT solution and sonicated for another 10 min to produce a well-dispersed HNT-CNT–SA mixture.

Preparation of the HNT-Photothermal Hydrogel: The HNT—CNT–SA dispersion was transferred into a cylindrical PTFE mold (diameter: 3 cm) and placed on the surface of a copper block under liquid nitrogen. After the dispersion was fully frozen, it was freeze-dried for 24 h to obtain the initial aerogel. The freeze-dried aerogel was then immersed into a 5.0 wt.% $AlCl_3$ solution for 48 h to form an Al^{3+} cross-linked HNT-photothermal hydrogel. The hydrogel was washed with water to remove any residual Al^{3+}. The diameter of the hydrogel after cross-linking decreased to 2.7 cm.

Characterizations: The morphologies of the HNT-, BN-, and ZL-based aerogels were investigated by SEM (Zeiss, GEMINI 2) and TEM (JEOL, JEM-2100). XRD data were collected on an X-ray diffractometer (D8 Advance, Bruker) with Cu Kα radiation (λ = 1.5418 Å). FTIR spectra were recorded with an FTIR spectrometer (PerkinElmer, Llantrisant, UK). The composition and surface oxidation state were probed by XPS (Kratos Analytical, Manchester, United Kingdom). Raman spectroscopy was performed using a Via-Reflex spectrometer 309 (Renishaw) with a laser excitation wavelength of 532 nm. The laser power was 5%. The concentrations of different ions were measured by ICP-OES (Agilent 7500). Heat flow was recorded by DSC analysis (TA instruments Discovery TGA/DSC). UV–vis spectra were recorded using a UV-3600 Spectrometer (Shimadzu). A contact angle system (Dataphysics OCA 20) was utilized to investigate the hydrophilicity. The LF-NMR analyzer (NMI20-030H-I, Shanghai Niumag Corporation, Shanghai, China) was used to obtain the T_2 relaxation spectra. The resonance frequency was 12 MHz and the T_2 relaxation spectra were measured with CPMG sequence. The ^{1}H chemical shift was obtained from nuclear magnetic resonance imaging (NMR) spectroscopy by Bruker advance III 600 Plus system.

Solar-Driven Steam Generation: Indoor evaporation testing was conducted under laboratory conditions with a constant ambient temperature of 25 °C and a humidity of 32%. A Newport Oriel Solar Simulator (Model: 69 907) was used as the light source. A white PS foam with a hole was employed to hold the hydrogel evaporator and cover the water surface. The mass change of water/seawater was recorded by an electronic balance (Videos S1 and S2, Supporting Information). The mass change of water/seawater was recorded by an electronic balance. An infrared (IR) camera (FLIR E64501) was used to monitor the surface temperature of evaporators. Natural seawater for evaporation tests was collected from the Adelaide Sea Semaphore Beach (Note S14, Supporting Information).

The DFT-Based AIMD Simulations: The DFT-based AIMD simulations of the ion exchange process were performed using the CP2K package.[64,65] The PBE functional and Kohn–Sham DFT were used to describe the system and electronic structure in the framework of the Gaussian and plane waves methods, respectively. The DZVP basis set along with Goedecker–Teter–Hutter (GTH) pseudopotential and PBE functional with Grimme D3 dispersion correction was used. A plane-wave energy cut-off and relative cut-off of 500 and 60 Ry were employed, respectively. The simulation boxes were set to 20.8 × 18.1 × 30.0 Å^3. The simulations were carried out at 350 K temperature. The NVT ensemble was used with a CSVR thermostat, and the time step was set to 1 fs.

The adsorption energy and bond dissociation energy calculations between different ions and HNTs were also carried out with the CP2K package. The GTH pseudopotentials and DZVP-MOLOPT-SR-GTH basis set were conducted. A plane-wave energy cut-off and relative cut-off of 500 and 60 Ry were employed, respectively. The energy convergence criterion was set to 10–6 Hartree. Geometry optimization for the HNT (001) slab was carried out within a 20.8700 × 18.1442 × 30.0000 Å^3 box under a periodic boundary condition with dense Monkhorst–Pack k point meshes of 1 × 1 × 1. On the *Z*-direction, there was a 15 Å vacuum layer for avoiding the effect of periodic conditions for the slab model in the *z*-axis. Different ions were placed on the side with Al–O octahedron and the actual charge of various ions was taken into account during the whole geometry optimization process.

The adsorbed energy between the HNT slab and ions was defined as the following equation:

$$E_{ads-ion} = E_{HNT-slab+ion} - E_{HNT-slab} - E_{ion} \quad (1)$$

As for the dissociation energy, the structures of HNT with one Al atom substituted by different ions and losing one Al atom were optimized and compared by the following equation:

$$E_{dis} = E_{HNT-lose-Al} + E_{ion} - E_{HNT-sub-ion} \quad (2)$$

Molecular Dynamics Simulation: MD simulations were performed using the GROMACS software.[66] To integrate the equations of motion, a leapfrog integrator with a time step of 1 fs. A 1.0 nm cutoff distance was applied for both van der Waals and electrostatic interactions, while the particle mesh Ewald method was utilized to compute the electrostatic interactions. In the NVT simulations, the V-rescale thermostat with a characteristic time of 2 ns was implemented to maintain a constant temperature, while in the NPT simulations, an isotropic Parrinello Rahman barostat was used to maintain a pressure of 1 atm. The cubic box with periodic boundary conditions had dimensions of 7.0 × 7.0 × 7.0 nm^3. The simulation systems consisted of 8593 water molecules, 10 cations (K^+, Na^+, Ca^{2+}, or Mg^{2+}), and 10 Cl^- for the NaCl and KCl systems, or 20 Cl^- for the $CaCl_2$ or $MgCl_2$ systems. The OPC3[67] water model was utilized, and the ion interaction parameters were taken from the Merz force field.[68] Four simulation systems were run for 20 ns to ensure equilibrium was achieved, and the last 5 ns of the equilibrium state was used for final analysis. The hydrogen bond (HB) calculation was based on the geometrical configuration in which the distance between two O atoms was <3.5 Å and the angle of O—H···O was <30°.

The evaporations of pure water and seawater on unmodified HNT surfaces and ion-modified HNT surfaces were also studied by molecular dynamics simulation. The Forcite Plus module in Materials Studio was used to set up the pure water and seawater systems through the Amorphous Cell module. The solution surface and HNT surfaces were spliced through a build layer, in which the number of water molecules was 500. Before dynamic evaporation simulation, the model energy was minimized by geometric optimization. Among them, the force field was the Universal Force field, and the charge distribution method was charge equilibration. In order to study the non-bond interaction of the system, the Ewald tracing electrostatic summations method, and the Atom Based van der Waals summations method were applied. The total kinetic time was 200 ps, with a time step of 0.2 fs.

A facile and general strategy was developed to make real seawater evaporation faster than pure water. By simply introducing specific mineral materials into the floating photothermal evaporator, Mg^{2+} and Ca^{2+} ions in seawater were accumulated at the photothermal interfaces by spontaneous ion exchange, which directly disturbed the hydrogen bonds of water molecules, leading to a reduction in the evaporation enthalpy, and consequently achieved much higher seawater evaporation rates compared to pure water.

Supporting Information

Supporting Information is available from the Wiley Online Library or from the author.

Acknowledgements

H.Y., H.J., M.Q., and Y.L. contributed equally to this work. H.X. and G.O. acknowledge the financial support from the Australian Research Council (FT190100485, DP220100583, DP240101581). Y.W. and P.W. acknowledge financial support from the China Scholarship Council for primary scholarships and from the Future Industries Institute for top up scholarships. All authors acknowledge the use of the SA node of the NCRIS-enabled Australian National Fabrication Facility (ANFF). The authors thank Dr Rong

Fan from CSIRO for initially providing the authors with HNTs that led to notice that the seawater evaporates faster than freshwater. The authors also thank A/Prof. Yao Zheng and Prof. Shizhang Qiao from the University of Adelaide for assistance with Raman characterization.

Conflict of Interest

The authors declare no conflict of interest.

Data Availability Statement

The data that support the findings of this study are available from the corresponding author upon reasonable request.

Keywords

desalination, interfacial solar evaporation, ion exchange, photothermal, seawater evaporation

Received: September 17, 2024
Revised: October 27, 2024
Published online:

[1] T. Oki, S. Kanae, *Science* **2006**, *313*, 1068.
[2] M. M. Mekonnen, A. Y. Hoekstra, *Sci. Adv.* **2016**, *2*, e1500323.
[3] M. Elimelech, W. A. Phillip, *Science* **2011**, *333*, 712.
[4] W. J. Koros, C. Zhang, *Nat. Mater.* **2017**, *16*, 289.
[5] W. Pronk, A. Ding, E. Morgenroth, N. Derlon, P. Desmond, M. Burkhardt, B. Wu, A. G. Fane, *Water Res.* **2019**, *149*, 553.
[6] S. Burn, M. Hoang, D. Zarzo, F. Olewniak, E. Campos, B. Bolto, O. Barron, *Desalination* **2015**, *364*, 2.
[7] P. Tao, G. Ni, C. Song, W. Shang, J. Wu, J. Zhu, G. Chen, T. Deng, *Nat. Energy* **2018**, *3*, 1031.
[8] Z. Wang, T. Horseman, A. P. Straub, N. Y. Yip, D. Li, M. Elimelech, S. Lin, *Sci. Adv.* **2019**, *5*, eaax0763.
[9] F. Wang, N. Xu, W. Zhao, L. Zhou, P. Zhu, X. Wang, B. Zhu, J. Zhu, *Joule* **2021**, *5*, 1602.
[10] W. Wang, S. Aleid, Y. Shi, C. Zhang, R. Li, M. Wu, S. Zhuo, P. Wang, *Joule* **2021**, *5*, 1873.
[11] H. Ghasemi, G. Ni, A. M. Marconnet, J. Loomis, S. Yerci, N. Miljkovic, G. Chen, *Nat. Commun.* **2014**, *5*, 4449.
[12] F. Zhao, Y. Guo, X. Zhou, W. Shi, G. Yu, *Nat. Rev. Mater.* **2020**, *5*, 388.
[13] X. Chen, N. Yang, Y. Wang, H. He, J. Wang, J. Wan, H. Jiang, B. Xu, L. Wang, R. Yu, L. Tong, L. Gu, Q. Xiong, C. Chen, S. Zhang, D. Wang, *Adv. Mater.* **2022**, *34*, 2107400.
[14] Y. Lu, D. Fan, Z. Shen, H. Zhang, H. Xu, X. Yang, *Nano Energy* **2022**, *95*, 107016.
[15] Y. Wang, X. Wu, P. Wu, J. Zhao, X. Yang, G. Owens, H. Xu, *Sci. Bull.* **2021**, *66*, 2479.
[16] X. Wu, Z. Wu, Y. Wang, T. Gao, Q. Li, H. Xu, *Adv. Sci.* **2021**, *8*, 2002501.
[17] S. C. Singh, M. ElKabbash, Z. Li, X. Li, B. Regmi, M. Madsen, S. A. Jalil, Z. Zhan, J. Zhang, C. Guo, *Nat. Sustainability* **2020**, *3*, 938.
[18] J. Zhou, S. Lin, H. Zeng, J. Liu, B. Li, Y. Xu, X. Zhao, G. Chen, *Mater. Horiz.* **2020**, *7*, 2936.
[19] H. Liu, Z. Huang, K. Liu, X. Hu, J. Zhou, *Adv. Energy Mater.* **2019**, *9*, 1900310.
[20] F. Zhao, X. Zhou, Y. Shi, X. Qian, M. Alexander, X. Zhao, S. Mendez, R. Yang, L. Qu, G. Yu, *Nat. Nanotechnol.* **2018**, *13*, 489.
[21] X. Li, J. Li, J. Lu, N. Xu, C. Chen, X. Min, B. Zhu, H. Li, L. Zhou, S. Zhu, T. Zhang, J. Zhu, *Joule* **2018**, *2*, 1331.
[22] Z. Xu, L. Zhang, L. Zhao, B. Li, B. Bhatia, C. Wang, K. L. Wilke, Y. Song, O. Labban, J. H. Lienhard, R. Wang, E. N. Wang, *Energy Environ. Sci.* **2020**, *13*, 830.
[23] Y. Guo, G. Yu, *ACS Mater. Lett.* **2022**, *4*, 713.
[24] C. Lei, W. Guan, Y. Guo, W. Shi, Y. Wang, K. P. Johnston, G. Yu, *Angew. Chem., Int. Ed.* **2022**, *61*, e202208487.
[25] J. Xu, G. Wang, L. Zhu, G. Jiang, Y. Lei, Z. Zeng, L. Xue, *Chem. Eng. J.* **2023**, *455*, 140704.
[26] P. Zhang, F. Zhao, W. Shi, H. Lu, X. Zhou, Y. Guo, G. Yu, *Adv. Mater.* **2022**, *34*, 2110548.
[27] X. Zhou, F. Zhao, Y. Guo, Y. Zhang, G. Yu, *Energy Environ. Sci.* **2018**, *11*, 1985.
[28] J. Han, W. Xing, J. Yan, J. Wen, Y. Liu, Y. Wang, Z. Wu, L. Tang, J. Gao, *Adv. Fiber Mater.* **2022**, *4*, 1233.
[29] Y. Zhang, Z. Huang, Z. Cai, Y. Ye, Z. Li, F. Qin, J. Xiao, D. Zhang, Q. Guo, Y. Song, J. Yang, *Sci. Adv.* **2021**, *7*, eabi7498.
[30] H. Liu, B. Chen, Y. Chen, M. Zhou, F. Tian, Y. Li, J. Jiang, W. Zhai, *Adv. Mater.* **2023**, *35*, 2301596.
[31] B. Lv, C. Gao, Y. Xu, X. Fan, J. Xiao, Y. Liu, C. Song, *Desalination* **2021**, *510*, 115093.
[32] X. Wang, Z. Li, X. Wu, B. Liu, T. Tian, Y. Ding, H. Zhang, Y. Li, Y. Liu, C. Dai, *Polymers* **2024**, *16*, 2231.
[33] Q. Xia, C. Wang, N. Xu, J. Yang, G. Gao, J. Ding, *Adv. Funct. Mater.* **2023**, *33*, 2214769.
[34] S. Tian, Z. Huang, J. Tan, X. Cui, Y. Xiao, Y. Wan, X. Li, Q. Zhao, S. Li, C.-S. Lee, *ACS Energy Lett.* **2020**, *5*, 2698.
[35] C. Ma, Q. Liu, Q. Peng, G. Yang, M. Jiang, L. Zong, J. Zhang, *ACS Nano* **2021**, *15*, 19877.
[36] X. Su, D. Hao, M. Sun, T. Wei, D. Xu, X. Ai, X. Guo, T. Zhao, L. Jiang, *Adv. Funct. Mater.* **2022**, *32*, 2108135.
[37] Z. Yu, R. Gu, Y. Tian, P. Xie, B. Jin, S. Cheng, *Adv. Funct. Mater.* **2022**, *32*, 2108586.
[38] S. Cao, P. Rathi, X. Wu, D. Ghim, Y.-S. Jun, S. Singamaneni, *Adv. Mater.* **2021**, *33*, 2000922.
[39] X. Dong, L. Cao, Y. Si, B. Ding, H. Deng, *Adv. Mater.* **2020**, *32*, 1908269.
[40] Y. Guo, C. M. Dundas, X. Zhou, K. P. Johnston, G. Yu, *Adv. Mater.* **2021**, *33*, 2102994.
[41] Y. Zheng, R. A. Caceres Gonzalez, K. B. Hatzell, M. C. Hatzell, *Joule* **2021**, *5*, 1971.
[42] J. Chen, J. L. Yin, B. Li, Z. Ye, D. Liu, D. Ding, F. Qian, N. V. Myung, Q. Zhang, Y. Yin, *ACS Nano* **2020**, *14*, 17419.
[43] Z. Liu, Z. Zhou, N. Wu, R. Zhang, B. Zhu, H. Jin, Y. Zhang, M. Zhu, Z. Chen, *ACS Nano* **2021**, *15*, 13007.
[44] Y. Lu, D. Fan, Y. Wang, H. Xu, C. Lu, X. Yang, *ACS Nano* **2021**, *15*, 10366.
[45] H. Yang, Y. Sun, M. Peng, M. Cai, B. Zhao, D. Li, Z. Liang, L. Jiang, *ACS Nano* **2022**, *16*, 2511.
[46] W. Zhao, H. Gong, Y. Song, B. Li, N. Xu, X. Min, G. Liu, B. Zhu, L. Zhou, X.-X. Zhang, J. Zhu, *Adv. Funct. Mater.* **2021**, *31*, 2100025.
[47] Y. Zhou, Q. Lu, Q. Liu, H. Yang, J. Liu, J. Zhuang, W. Shi, X. Wang, *Adv. Funct. Mater.* **2021**, *32*, 2112159.
[48] Y. Kuang, C. Chen, S. He, E. M. Hitz, Y. Wang, W. Gan, R. Mi, L. Hu, *Adv. Mater.* **2019**, *31*, 1900498.
[49] Y. Zhang, T. Xiong, D. K. Nandakumar, S. C. Tan, *Adv. Sci.* **2020**, *7*, 1903478.
[50] L. Li, N. He, B. Jiang, K. Yu, Q. Zhang, H. Zhang, D. Tang, Y. Song, *Adv. Funct. Mater.* **2021**, *31*, 2104380.
[51] L. Zhang, X. Li, Y. Zhong, A. Leroy, Z. Xu, L. Zhao, E. N. Wang, *Nat. Commun.* **2022**, *13*, 849.
[52] L. Wu, Z. Dong, Z. Cai, T. Ganapathy, N. X. Fang, C. Li, C. Yu, Y. Zhang, Y. Song, *Nat. Commun.* **2020**, *11*, 521.
[53] C. Zhang, Y. Shi, L. Shi, H. Li, R. Li, S. Hong, S. Zhuo, T. Zhang, P. Wang, *Nat. Commun.* **2021**, *12*, 998.

[54] X. Wu, Y. Wang, P. Wu, J. Zhao, Y. Lu, X. Yang, H. Xu, *Adv. Funct. Mater.* **2021**, *31*, 2102618.
[55] D. W. Smith, *J. Chem. Educ.* **1977**, *54*, 540.
[56] J. Zhou, X. Lu, Y. Wang, J. Shi, *Fluid Phase Equilib.* **2002**, *194–197*, 257.
[57] K. J. Tielrooij, N. Garcia-Araez, M. Bonn, H. J. Bakker, *Science* **2010**, *328*, 1006.
[58] J. Eke, A. Yusuf, A. Giwa, A. Sodiq, *Desalination* **2020**, *495*, 114633.
[59] H. Zou, X. Meng, X. Zhao, J. Qiu, *Adv. Mater.* **2023**, *35*, 2207262.
[60] S. Kumar, S. Jain, *J. Chem.* **2013**, *2013*, 957647.
[61] T. R. E. Kressman, *J. Phys. Chem.* **1952**, *56*, 118.
[62] Y. Jin, J. Chang, Y. Shi, L. Shi, S. Hong, P. Wang, *J. Mater. Chem. A* **2018**, *6*, 7942.
[63] L. Zhou, Y. Tan, J. Wang, W. Xu, Y. Yuan, W. Cai, S. Zhu, J. Zhu, *Nat. Photonics* **2016**, *10*, 393.
[64] J. VandeVondele, M. Krack, F. Mohamed, M. Parrinello, T. Chassaing, J. Hutter, *Comput. Phys. Commun.* **2005**, *167*, 103.
[65] J. Hutter, M. Iannuzzi, F. Schiffmann, J. VandeVondele, *Wiley Interdiscip. Rev.: Comput. Mol. Sci.* **2014**, *4*, 15.
[66] H. J. C. Berendsen, D. van der Spoel, R. van Drunen, *Comput. Phys. Commun.* **1995**, *91*, 43.
[67] S. Izadi, A. V. Onufriev, *J. Chem. Phys.* **2016**, *145*, 074501.
[68] Z. Li, L. F. Song, P. Li, K. M. Merz, *J. Chem. Theory Comput.* **2020**, *16*, 4429.